Available online at www.sciencedirect.com

SciVerse ScienceDirect

Ceramics International 38 (2012) 5651–5659

CERAMICS INTERNATIONAL

www.elsevier.com/locate/ceramint

Effects of electrolyte pattern on mechanical and electrochemical properties of solid oxide fuel cells

Bora Timurkutluk [a,b,*], Selahattin Celik [a,c], Serkan Toros [a], Cigdem Timurkutluk [a,b], Mahmut D. Mat [a], Yuksel Kaplan [a]

[a] Nigde University, Mechanical Engineering Department, 51245 Nigde, Turkey
[b] Vestel Defense Industry, Silicon Block, ZK 14, ODTU Teknokent, 06531 Ankara, Turkey
[c] Gazi University, Mechanical Engineering Department, 06570 Ankara, Turkey

Received 7 March 2012; received in revised form 2 April 2012; accepted 2 April 2012
Available online 11 April 2012

Abstract

In order to enhance the electrochemical performance and reduce the operation temperature of a conventional electrolyte supported solid oxide fuel cell (SOFC), a three layered electrolyte with various geometry is designed and fabricated. Novel three layered electrolytes comprise a dense and thin scandia alumina stabilized zirconia (ScAlSZ) electrolyte layer sandwiched between two hallow ScAlSZ electrolyte layers each having the same thickness as the support but machined into a filter like architecture in the active region with circular, rectangular and triangular cut off patterns. The percent of thin electrolyte layer in the active region is kept constant as 30% for all designs in order to investigate the effect of pattern geometry on the mechanical properties and the performance of the electrolytes. Single cells based on novel electrolytes are manufactured and electrochemical properties are evaluated. A standard electrolyte and electrolyte supported cell are also fabricated as a base case for comparison. Although the electrolyte having triangular patterns has the highest peak power at all operation temperatures considered, it exhibits the lowest flexural strength.

Keywords: Solid oxide fuel cell; Scandia alumina stabilized zirconia; Novel electrolyte design; Bending strength

1. Introduction

The lowering of SOFC operation temperature is one of the major issues in the aspect of cost reduction, long service life and commercialization of the SOFC systems. With the development of thin film technologies, it is possible to fabricate 5–10 μm thin electrolytes deposited generally on the anode in order to reduce the operation temperature by employing tape casting and co-sintering [1–4] or surface coating methods, such as vapor deposition [5–9], laser deposition [10–12] and electrophoretic deposition [13–15]. In spite of having excellent features such as excellent catalytic activity and good mechanical properties as an SOFC anode, Ni-based anodes suffer from the cyclic reduction and oxidation (redox) which is likely to occur during the lifetime of the SOFC system. The volumetric changes due to Ni–NiO–Ni cycle may seriously damage the anode network [16–18]. The damage accumulates with the increasing redox cycles leading to significant performance loss and mechanical failure [19–21]. In this respect, the anode supported design especially is more vulnerable to redox cycling due to thick anode support. The cell failure due to cracked electrolyte is reported even after only few redox cycles for anode supported cells [22–24]. The electrolyte supported design, on the other hand, is less susceptible to failure during redox cycling and serves relatively strong structure however suffers from low performance due to thick electrolyte.

The electrolyte material has also great influence on the SOFC operation temperature. In the state of art SOFCs, yttria stabilized zirconia (YSZ) is the most common electrolyte material. Although YSZ is purely ionic conductive [25–27] and has very good chemical stability under SOFC operation conditions [28–30], YSZ supported SOFCs require high operation temperature around 800–1000 °C which is essential

* Corresponding author at: Nigde University, Mechanical Engineering Department, 51245 Nigde, Turkey. Tel.: +90 388 225 23 37; fax: +90 388 225 01 12.
E-mail address: bora.timurkutluk@nigde.edu.tr (B. Timurkutluk).

0272-8842/$36.00
http://dx.doi.org/10.1016/j.ceramint.2012.04.008

to reach acceptable ionic conductivity [31,32]. Gadolinium/samarium doped ceria (GDC/SDC), strontium and magnesium doped lanthanum gallate (LSGM) and scandia stabilized zirconia (ScSZ) are alternative electrolyte materials exhibiting high ionic conductivities at relatively low operation temperatures compared to YSZ. In spite of high ionic conductivity at lower temperatures, GDC/SDC gains some electronic conductivity at reducing conditions during the SOFC operation due to reduction of cerium ions from Ce^{4+} to Ce^{3+} [33–35]. The volume change during this reduction leads to significant structural problems together with power loss due to short circuit [36–38]. LSGM reacts with NiO anode during the fabrication and operation of the cell. The formation of La–Ni phase deactivates the anode, thus a substantial degradation in the anode and cell performances are reported [39–42]. ScSZ, on the other hand, has none of these significant drawbacks above and shows the highest ionic conductivity among all zirconia based SOFC electrolytes at lower temperatures [43–45].

The ionic conductivity of ScSZ is mainly depending on the dopant level and the maximum conductivity is obtained around 10 mol% scandia doping [46,47]. The addition of 10 mol% scandia also stabilizes the cubic structure. However, 10 mol% scandia stabilized zirconia suffers from the phase transition from the cubic to rhombohedral phase resulting in abrupt decrease in the ionic conductivity especially below 700 °C [48–50]. Attempts in the literature for further stabilizing the cubic phase showed that the aging phenomenon can be avoided with the addition of small amounts of ceria (CeO_2) [51–53] or alumina (Al_2O_3) [54,55]. Thus, scandia alumina stabilized zirconia is chosen as an electrolyte material in this study.

Although the cubic phase is highly conductive, it shows low mechanical performance due to grain growth during sintering. Thus, an approximately 150 μm thick electrolyte is required to support the whole cell mechanically. In that case, the ohmic resistance of electrolytes becomes the main contributor to the overall cell resistance for electrolyte supported SOFCs leading to significant performance loss [56–58].

The mechanical properties of an electrolyte need to be improved in order to avoid undesired effects of the thick electrolyte on the cell performance. The mechanical strength of cubic ScSZ can be enhanced by controlling the grain size determined mainly by the sintering method applied as well as the initial powder size. Small grains are required for higher mechanical strength. Hot pressing, spark plasma and microwave sintering are usually employed in the literature to suppress the grain growth of the electrolyte for improved mechanical properties. These techniques allow densification at relatively lower temperature and reduce the sintering time significantly compared to conventional sintering. Since the grain growth usually occurs during the final sintering stage at which the temperature is the highest, it is possible to overwhelm the grain growth by sintering at reduced temperature. Dahl et al. [59] investigated the densification of nanocrystalline YSZ powders by hot pressing at 1300 °C under 25 MPa and conventional sintering at 1500 °C. The grain size of the sample was measured as 0.37 and 12 μm after hot pressing and conventional sintering, respectively. The sample fabricated by hot pressing sintering exhibited higher fracture toughness than that of exposed to conventional sintering. Rajeswari et al. [60] studied the microstructure of ultra fine YSZ nano powder after spark plasma sintering under a pressure of 50 MPa. It was shown that it is possible to obtain fully dense YSZ electrolyte with an average grain size of around 80 nm after sintering only at 1050 °C.

Since the microwave sintering provides volumetric heating mechanism, a rapid and uniform sintering process occurs. Mazaheri et al. [61] compared the effects of microwave sintering and conventional sintering on the microstructural and mechanical properties of nano sized YSZ powders. The microwave sintering was reported to suppress the grain growth resulting in a finer microstructure with an average grain size of 0.9 μm. On the other hand, the average grain size of the YSZ sample subjected to conventional sintering was measured 2.14 μm. The specimen produced via microwave sintering exhibited two times higher fracture toughness than that of obtained from conventional sintering due to finer grain size. Although these three sintering techniques offer improved mechanical properties by suppressing the grain growth, reduced sintering time and energy, they are not suitable for large size or large scale fabrication.

In this study, the electrical resistance of ScAlSZ electrolyte is significantly reduced by fabricating partly reduced thickness electrolytes in the active region via conventional sintering. Novel electrolytes offer also an important reduction in the SOFC operation temperature. The effect of electrolyte pattern geometry on the mechanical properties of the electrolyte and electrochemical properties of the single cell is also investigated.

2. Experimental

2.1. Base cell fabrication

A block diagram of the base cell is illustrated in Fig. 1. The five-layered cell comprises anode current collecting layer (ACL), anode functional layer (AFL), electrolyte, cathode functional layer (CFL) and cathode current collecting layer (CCL) from the anode to the cathode side. The electrolyte is manufactured by tape casting and anode/cathode layers are coated by screen printing technique. The cell fabrication stages are given in Fig. 2.

2.1.1. Electrolyte fabrication for the base cell

ScAlSZ powders ($(Sc_2O_3)_{0.1}(AlO_2)_{0.01}(ZrO_2)_{0.89}$) purchased from Nextech Materials (Ohio, USA) are mixed with certain amount of dispersant (fish oil, Sigma–Aldrich, Munich,

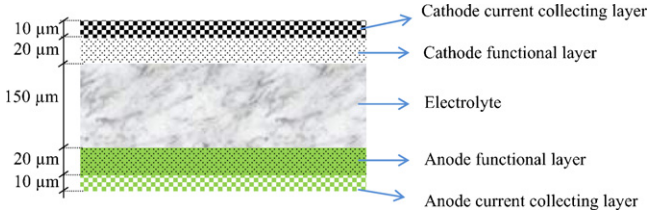

Fig. 1. The structure of the fabricated cell (not to scale).

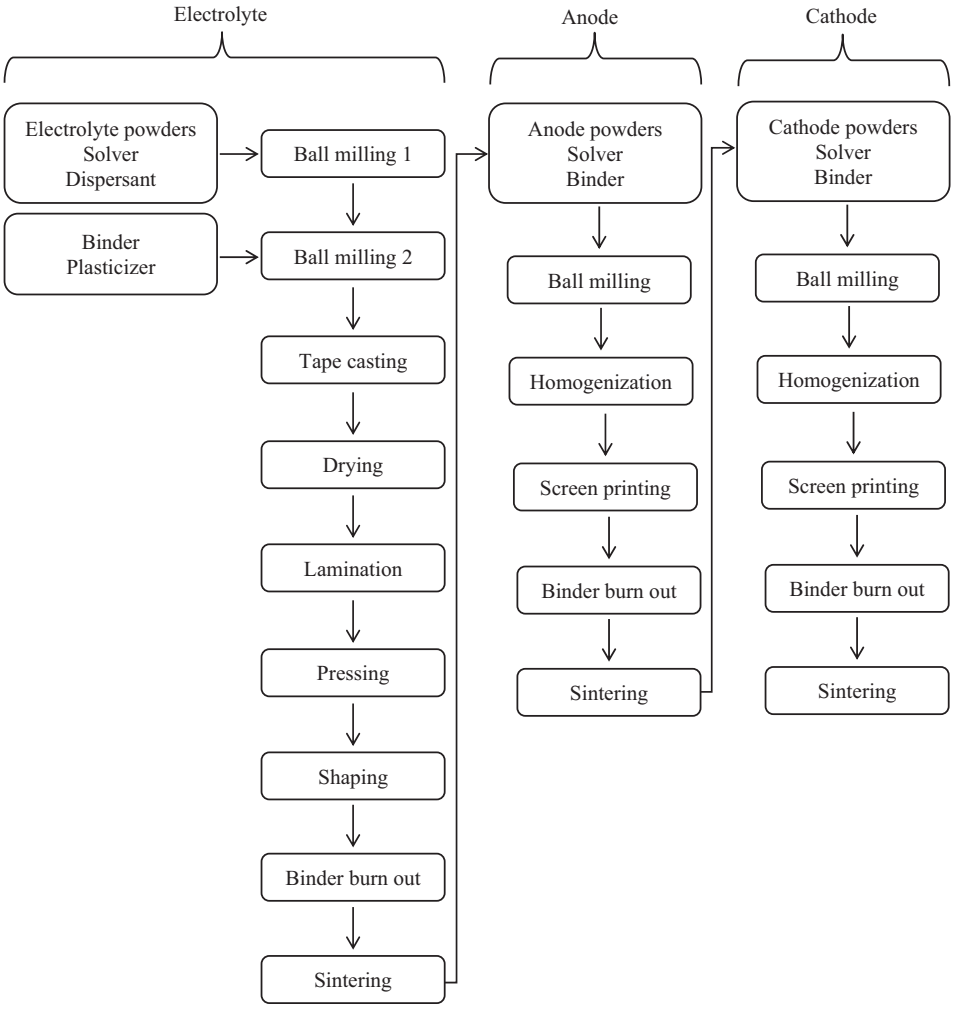

Fig. 2. The flow chart of the cell fabrication.

Germany) and solvent (ethanol, Sigma–Aldrich). After ball milling for around 24 h, organic binder (butvar, Sigma–Aldrich) and plasticizer (polyethylene glycol, Sigma–Aldrich) are added with suitable ratios. The mixture is ball milled again for another 24 h and then tape cast on a mylar strip with a blade gap of 170 μm. Six tapes are stacked and pressed isostatically under 40 MPa for 10 min. After shaping by a laser cutter in the form of a 78 mm × 78 mm, the electrolyte is heated to 1000 °C for 2 h to remove the organic additions. Pre-sintered electrolyte is then moved to the high temperature furnace to obtain fully dense electrolyte. After sintering at 1400 °C for 5 h, the thickness of the base cell electrolyte after sintering is measured as 150 μm whereas the final outer dimensions are 60 × 60 mm.

2.1.2. Fabrication of novel electrolytes

Three sets of two layered electrolyte laminate are fabricated similar to the base cell electrolyte fabrication. Two of them are machined by a laser cutter in a grate like architecture in the active region with circular, rectangular and triangular cut off patterns. The third one is then sandwiched symmetrically between two machined thin electrolytes (at the center in Fig. 3). After isostatic pressing at 40 MPa for 10 min, electrolytes are sintered similar to that applied for the base cell electrolyte. The thickness of the thin electrolyte and both machined electrolytes was around 50 μm.

Three different novel electrolytes (electrolytes A–C) belonging to Cells A–C are designed and fabricated. The percent of thin electrolyte layer in the active region is kept constant as 30% for all electrolyte designs. Their technical drawings and photos after the isostatic press are given in Fig. 3.

2.1.3. Fabrication of electrodes

NiO-F powders (Novamet, New Jersey, USA) are mixed with ScAlSZ powders corresponding to a weight ratio of 3:2, respectively. An appropriate amount of ethyl cellulose binder and terpineol solvent (both from Sigma–Aldrich) are also added in order to prepare screen printable AFL slurry. After ball milling for around 12 h and homogenization via a three rolls mill, AFL is screen printed on the electrolyte. The screen printing paste for the ACL layer is prepared similarly. NiO-A powders purchased from Novamet are mixed with ethyl cellulose and terpineol at suitable ratios. Activated charcoal obtained from Sigma–Aldrich is also added as a pore former at a weight of 10 wt.% of NiO-A powders. After ball milling for

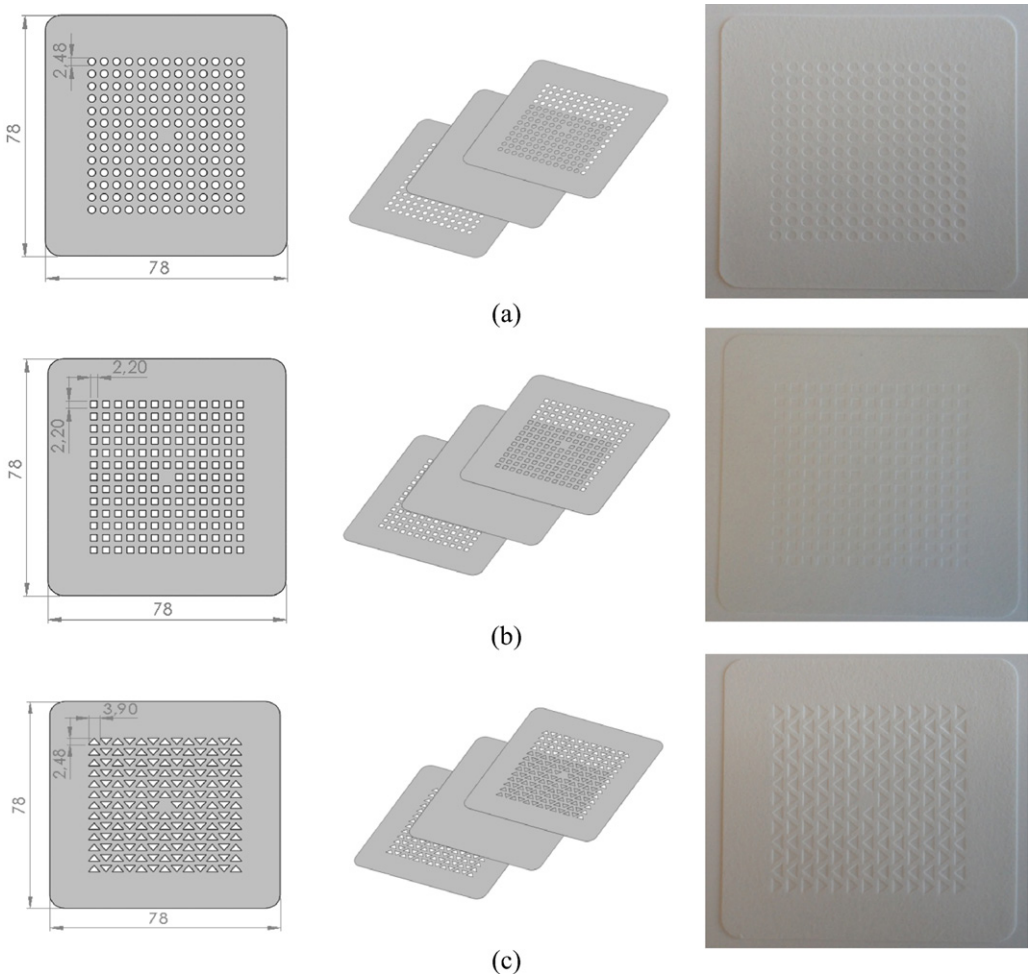

Fig. 3. Technical drawings (left), structure (center) and photos (right) of grate type electrolytes: (a) Cell A, (b) Cell B and (c) Cell C (all dimensions are in mm).

around 12 h and homogenization via a three rolls mill, the ACL paste is screen printed on the AFL previously dried at 100 °C for 30 min. Both anode layers are then co-sintered at 1250 °C for 3 h. The active anode area is adjusted to 16 cm^2 (4 × 4 cm) for all cells fabricated. Similarly, LSF ($La_{0.60}Sr_{0.40}FeO_{3-d}$, Nextech Materials)/ScAlSZ (wt.% 50/50) cathode functional layer and LSF cathode current collecting layer are coated on the other side of the electrolyte with the same active area of 16 cm^2 for all cells fabricated. Both cathode layers are co-sintered at 1000 °C for 2 h. The thicknesses of the functional and current collecting layers are controlled by the number of the passes performed by the printing machine. After sintering, thicknesses of AFL/CFL and ACL/CCL are measured from the uncoated electrolyte surface as 20 μm and 10 μm, respectively.

2.2. Bending tests

The mechanical performance of thin sheet electrolyte material of ScAlSZ with different pattern was analyzed by applying three point bending test in order to compare the effects of created patterns on samples. The apparatus used for the test is represented in Fig. 4 schematically. The dimensions of the analyzed samples are prepared as 60 mm × 60 mm × 150 μm. Three point bending tests are performed on a testing machine (Shimadzu Autograph AG-IS, Kyoto, Japan) with a data acquisition maintained by a digital interface board utilizing a specialized computer program. The radius of both support cylinders is $R = 15$ mm and loading cylinder has $r = 5$ mm radius. The distance between supports is chosen as $L = 50$ mm and bending speed is 1 mm min^{-1} in order to see the fast crack. The load applied to the test specimen and the corresponding deflection is measured until the specimen fractured. The bending tests are performed seven times for each base and novel electrolytes in order to increase the reliability of the results.

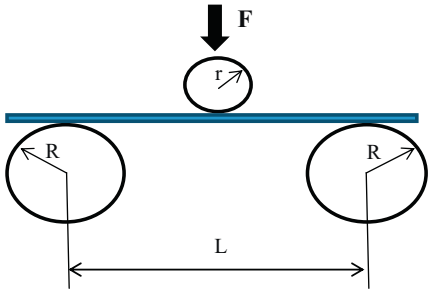

Fig. 4. Three point bending test bench.

2.3. Cell characterization

Fabricated single cells are sandwiched between two stainless steel interconnectors for the performance measurements. Silver ink (Nextech Materials) is applied as a current collecting paste for both electrodes. Then cells are placed in a temperature controlled furnace connected to the fuel cell test station (Arbin Instruments, FCTS, Texas, USA). The furnace has also a push rod pressing capability for better current collection. The anode side of cells is firstly purged with nitrogen until the operation temperature is reached and then reduced by hydrogen for half an hour. The cell performance is measured from 700 and 800 °C with hydrogen as a fuel and air as an oxidant. The microstructural properties of the cells are investigated via a scanning electron microscope (Carl Zeiss, Evo 40, London, England) while impedance measurements are through an impedance analyzer (Solartron Analytical, 1260A, Hempshire, UK) in a frequency range of 0.1 Hz–250 kHz at the open circuit potential.

3. Result and discussion

3.1. Microstructure

The microstructural images captured from the electrolyte belonging to Cell A are shown in Fig. 5 (a)–(c). Fig. 5(a) shows the surface microstructure of the electrolyte A. The grain size of the electrolyte is measured as between 0.3 and 2 μm. The cross sectional images captured from electrolyte A are shown in Fig. 5(b) and (c). It is seen that upper and bottom parts are well bonded to the support layer in the middle. The whole electrolyte has crack and delamination free structure. The cross section of Cell A, on the other hand, is given in Fig. 5(d). It is seen that the electrolyte was able to keep its crack and delamination free structure even after the coating of both electrode layers. The thickness of the thin electrolyte is measured as around 50 μm. Both electrodes seem to be porous as desired and well adhered to the electrolyte. No formation of secondary phases is observed between the electrolyte and both electrodes.

3.2. Mechanical characterization

Fig. 6 shows the load–displacement curves of electrolyte specimens with different patterns. It is seen that the base case electrolyte has the maximum displacement and load values followed by rectangular, triangular and circular patterns in an order. Although the increment rate of the force level with displacement for the electrolyte B is higher than those of electrolytes A and C, more deflection was obtained from the electrolyte A which has circular patterns. However, the minimum deflection was obtained from the electrolyte C. A possible explanation for obtaining the minimum deflection from the electrolyte C may be more stress concentration on the tips of the triangles.

The photos of fracture surfaces of the specimens are shown in Fig. 7. It is clearly seen that the crack firstly occurred at the thin parts of the electrolyte and then develops throughout the bending line for electrolyte A, corner tips of electrolytes B

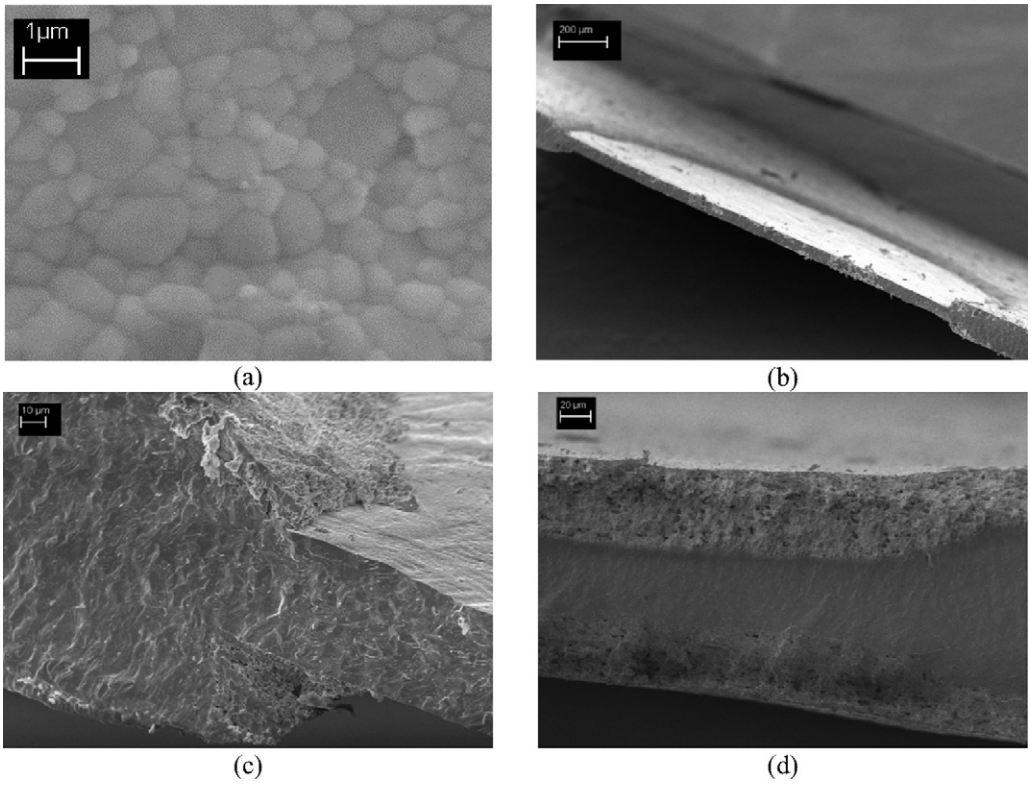

Fig. 5. Microstructures of the electrolyte belonging to Cell A (a–c) and cross section of Cell A.

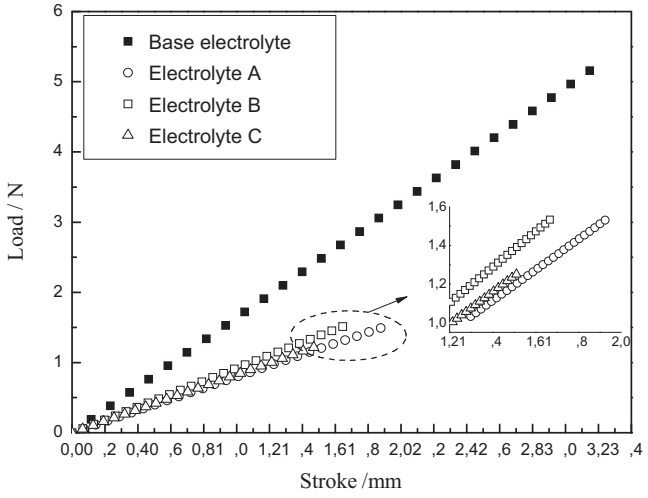

Fig. 6. Load–displacement curves of novel electrolytes.

and C as shown in the figure. These tips in the electrolytes B and C accelerate the progressing of the crack and reduce the strength.

The three point bending stress is a mechanical parameter for brittle material and defined as a material's ability to resist deformation under load which is also called as flexural strength or modulus of rupture (MOR). This stress can be calculated by using the following equation [62]:

$$\text{Stress}\,\sigma\,(\text{MPa}) = \frac{3lF}{2wt^2} \tag{1}$$

where l is the distance between the supports, F is the applied load, w is the width and t is the thickness of the specimen. The equation given above is only valid for the specimens that have the uniform cross sectional area. The original form of the equation is given as follows:

$$\text{Stress}\,\sigma\,(\text{MPa}) = \frac{Mc}{I} = \frac{Flt}{8I} \tag{2}$$

where I is the moment of inertia. Since the maximum deflection was obtained at the center of the specimens, all moments of inertias are calculated according to the mid plane of the specimens. The specimens' moments of inertia that have different patterns are different than that of the specimen with no pattern and they are determined as 0.016875 mm^4 for the mid plane of the base electrolyte and approximately 0.0163975 mm^4 for the mid plane of the patterned specimens. The calculated flexural strengths for the mid-plane and mid-point of specimens in which there is no pattern are illustrated in Fig. 8. It is seen that the maximum flexural strength was obtained from the base electrolyte and the electrolyte C exhibited the lowest flexural strength due to the notch effect as expected.

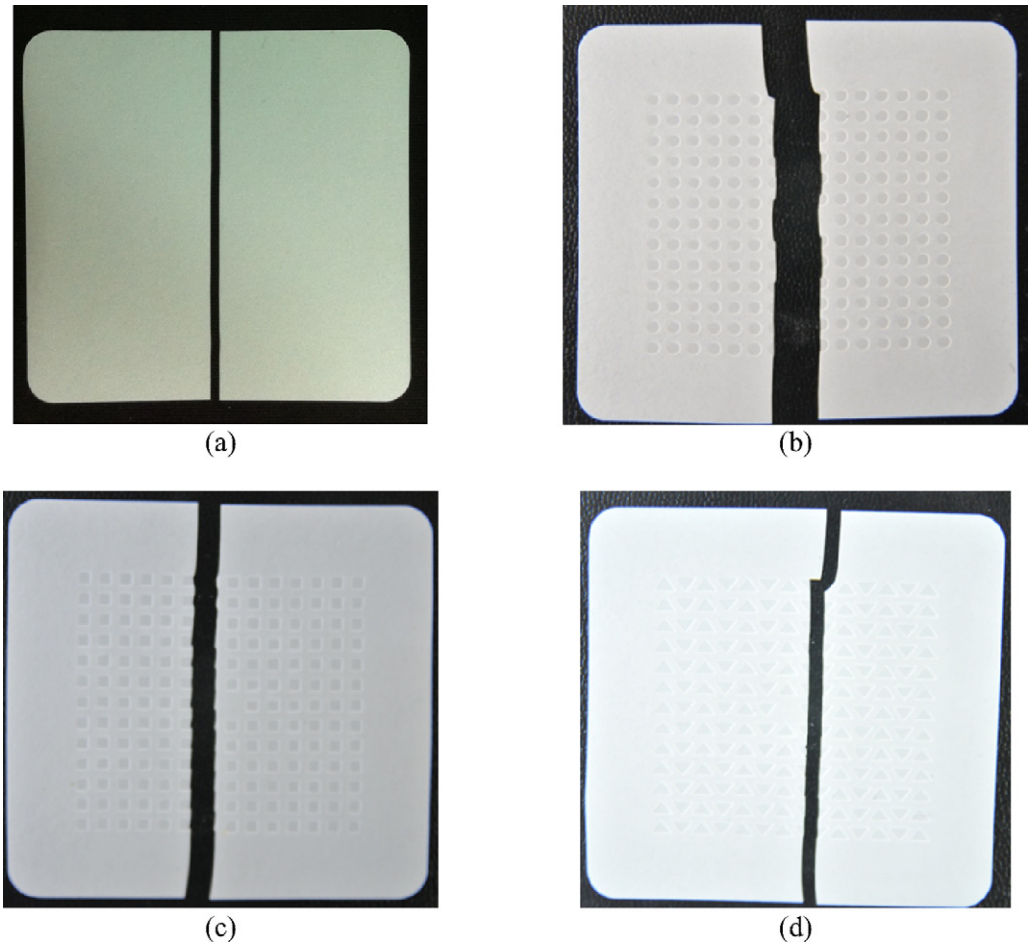

Fig. 7. Fracture surfaces of electrolyte A (a), B (b) and C (c).

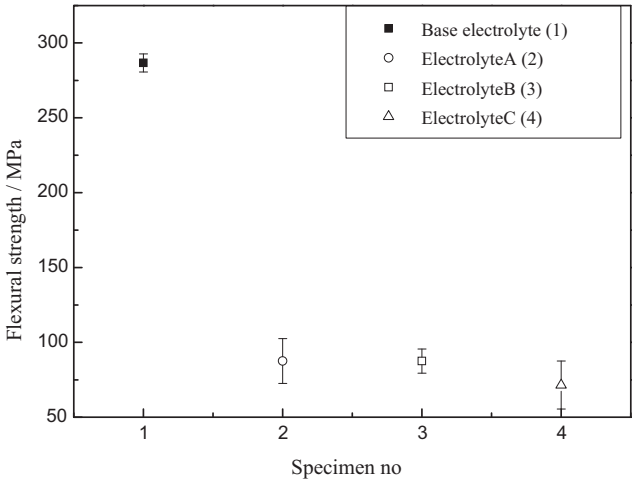

Fig. 8. Calculated flexural strength of novel electrolytes.

3.3. Electrochemical characterization

The performances of the fabricated cells at 750 °C operation temperature are depicted in Fig. 9. It is seen that all cells having novel electrolytes exhibited higher performance than the base case. 0.4, 0.54, 0.55 and 0.57 W cm^{-2} peak power densities were obtained from the base cell and Cells A–C, respectively. Furthermore, the base cell and Cells A–C exhibited 0.38, 0.49, 0.48 and 0.5 W cm^{-2} power densities, respectively, at an operation voltage of 0.7 V. The improvement about 50% in the performance is attributed to the partly reduced thickness of the electrolyte acquired by the novel design. Although Cell A and Cell B showed very similar performance characteristics, the performance of Cell C was slightly higher than those of Cell A and Cell B.

Impedance results revealed that it is mainly due to difference in the electrode resistance (Fig. 10). Impedance result for Cell B is not shown in the figure in order to avoid confusion since it is very similar to that of Cell A. It is seen that the ohmic resistances of Cell A and Cell C is very similar since they have the same percent of thin electrolyte in the active region. However, the electrode resistance of Cell C is slightly lower

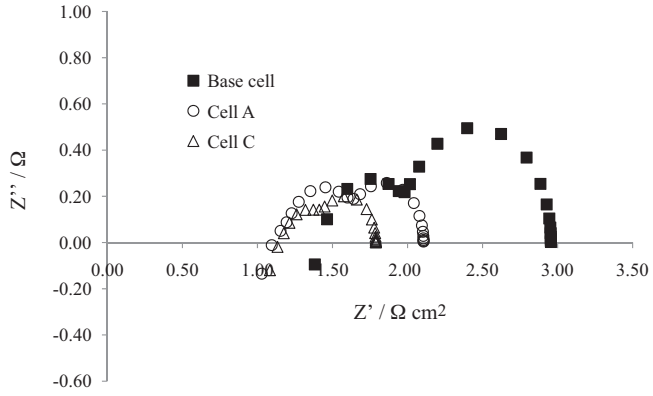

Fig. 10. Impedance comparison of cells at 750 °C.

than that of Cell A explaining the higher performance that Cell C shows. A possible explanation for this behavior may be the differences in the contact area between the both electrodes and the electrolytes which is directly related to the three phase boundaries. Although the percent of the thin membrane is the same for all cases, the lateral and rim surface area of the subtracted parts varies. The total electrode/electrolyte contact area for Cell A is calculated as 530.32 mm^2 while it is 545.94 mm^2 for Cell C. This result indicated that the electrolyte cut off patterns have also an influence on the cell performance in addition to mechanical properties.

Impedance data also showed that the improvement in the cell performance is as a result of the decrease in the electrolyte and electrode resistances achieved by the novel electrolyte design. The ohmic resistance of the base cell was measured as approximately 1.5 Ω cm^2 whereas it was about 1.1 Ω cm^2 for Cell A and Cell C. Similarly, the electrode resistance of the base cell seems to be higher than those measured for Cell A and Cell C.

Since the thickness of the electrolyte is reduced, the operation temperature is also expected to be lower. A typical example is given in Fig. 11 which shows the performance comparison of Cell C and the base cell. It is seen that Cell C produces 0.57 W cm^{-2} peak power density at an operation temperature of 750 °C whereas the base case exhibits the

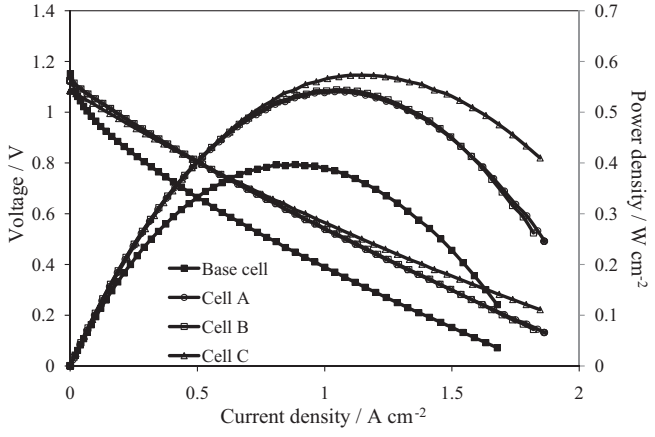

Fig. 9. Performance comparison of cells at 750 °C.

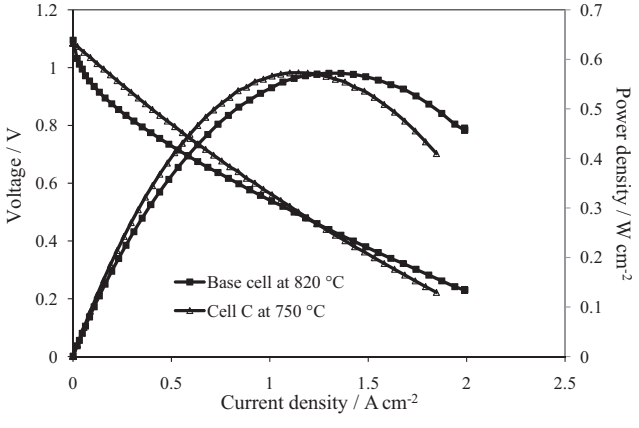

Fig. 11. Performance comparison of the base cell at 820 °C and Cell C at 750 °C.

same power output at an operation temperature of 820 °C. It can be concluded that suggested novel electrolyte design of Cell C also offers 70 °C reduction in the operation temperature as well.

4. Conclusions

Three different novel electrolytes having thin parts in the active region with circular, rectangular and triangular cut off patterns are designed and manufactured. The percent of thin electrolyte in the active region is kept as 30% for all cases in order to investigate the effect of cut off pattern geometry on the mechanical properties of the electrolyte and electrochemical performance of the cell. Three point bending tests showed that the electrolyte having triangular patterns has the lowest flexural strength due to notch effect which can be reduced by filleting the tips. All cells supported by novel electrolytes produced higher power than that of the standard electrolyte supported cell due to decrease in both electrolyte and electrode resistance indicated by impedance measurements. However, the cell having triangular patterned electrolyte exhibited the highest power output since it offers the highest electrolyte/electrode contact surface area. Impedance analysis confirmed that the electrode resistances were decreased as a result of the increase in the number of three phase boundaries. Moreover, the base cell showed the same peak power at 820 °C as produced by the cell having triangular cut off patterns at 750 °C. Therefore, the novel electrolytes also provide a significant reduction in the operation temperature which possibly improves the service life of the SOFC systems.

References

[1] C. Wang, L. Luo, Y. Wu, B. Hou, L. Sun, A novel multilayer aqueous tape casting method for anode-supported planar solid oxide fuel cell, Materials Letters 65 (2011) 2251–2253.

[2] S. Le, K.N. Sun, N. Zhang, X. Zhu, H. Sun, Y.X. Yuan, X. Zhou, Fabrication and evaluation of anode and thin Y_2O_3-stabilized ZrO_2 film by co-tape casting and co-firing technique, Journal of Power Sources 195 (2010) 2644–2648.

[3] H.G. Park, H. Moon, S.C. Park, J.J. Lee, D. Yoon, S.H. Hyun, D.H. Kim, Performance improvement of anode-supported electrolytes for planar solid oxide fuel cells via a tape-casting/lamination/co-firing technique, Journal of Power Sources 195 (2010) 2463–2469.

[4] C.M. Ana, J.H. Song, I. Kang, N. Sammes, The effect of porosity gradient in a nickel/yttria stabilized zirconia anode for an anode-supported planar solid oxide fuel cell, Journal of Power Sources 195 (2010) 821–824.

[5] B. Meng, X. He, Y. Sun, M. Li, Preparation of YSZ electrolyte coatings for SOFC by electron beam physical vapor deposition combined with a sol infiltration treatment, Materials Science and Engineering B 150 (2008) 83–88.

[6] H.Y. Jung, K.S. Hong, H. Kim, J.K. Park, J.W. Son, J. Kim, H.W. Lee, J.H. Lee, Characterization of thin-film YSZ deposited via EB-PVD technique in anode-supported SOFCs, Journal of the Electrochemical Society 153 (2006) A961–A966.

[7] G. Meng, H. Song, Q. Dong, D. Peng, Application of novel aerosol-assisted chemical vapor deposition techniques for SOFC thin films, Solid State Ionics 175 (2004) 29–34.

[8] K. Sasaki, M. Muranaka, A. Suzuki, T. Terai, Synthesis and characterization of LSGM thin film electrolyte by RF magnetron sputtering for LT-SOFCS, Solid State Ionics 179 (2008) 1268–1272.

[9] Y.L. Kuo, C. Lee, Y.S. Chen, H. Liang, Gadolinia-doped ceria films deposited by RF reactive magnetron sputtering, Solid State Ionics 180 (2009) 1421–1428.

[10] D. Yang, X. Zhang, S. Nikum, C.D. Petit, R. Hui, R. Maric, D. Ghosh, Low temperature solid oxide fuel cells with pulsed laser deposited bi-layer electrolyte, Journal of Power Sources 164 (2007) 182–188.

[11] K. Rodrigo, J. Knudsen, N. Pryds, J. Schou, S. Linderoth, Characterization of yttria-stabilized zirconia thin films grown by pulsed laser deposition (PLD) on various substrates, Applied Surface Science 254 (2007) 1338–1342.

[12] N. Pryds, B. Toftmann, J.B. Bilde-Sørensen, J. Schou, S. Linderoth, Thickness determination of large-area films of yttria-stabilized zirconia produced by pulsed laser deposition, Applied Surface Science 252 (2006) 4882–4885.

[13] T. Hosomi, M. Matsuda, M. Miyake, Electrophoretic deposition for fabrication of YSZ electrolyte film on non-conducting porous NiO–YSZ composite substrate for intermediate temperature SOFC, Journal of the European Ceramic Society 27 (2007) 173–178.

[14] S.M. Majhi, S.K. Behura, S. Bhattacharjee, B.P. Singh, T.K. Chongdar, N.M. Gokhale, L. Besra, Anode supported solid oxide fuel cells (SOFC) by electrophoretic deposition, International Journal of Hydrogen Energy 36 (2011) 14930–14935.

[15] M. Matsuda, T. Hosomia, K. Murata, T. Fukui, M. Miyake, Fabrication of bilayered YSZ/SDC electrolyte film by electrophoretic deposition for reduced-temperature operating anode-supported SOFC, Journal of Power Sources 165 (2007) 102–107.

[16] D. Sarantaridis, R.J. Chater, A. Atkinson, Changes in physical and mechanical properties of SOFC Ni–YSZ composites caused by redox cycling, Journal of the Electrochemical Society 155 (2008) B467–B472.

[17] C.M. Dikwal, W. Bujalski, K. Kendall, Characterization of the electrochemical performance of micro-tubular SOFC in partial reduction and oxidation conditions, Journal of Power Sources 181 (2008) 267–273.

[18] T. Hatae, Y. Matsuzaki, S. Yamashita, Y. Yamazaki, Current density dependence of changes in the microstructure of SOFC anodes during electrochemical oxidation, Solid State Ionics 180 (2009) 1305–1310.

[19] Q. Ma, F. Tietz, A. Leonide, E.I. Tiffée, Anode-supported planar SOFC with high performance and redox stability, Electrochemistry Communications 12 (2010) 1326–1328.

[20] B. Iwanschitz, J. Sfeir, A. Mai, M. Schütze, Degradation of SOFC anodes upon redox cycling: a comparison between Ni/YSZ and Ni/CGO, Journal of the Electrochemical Society 157 (2010) B269–B278.

[21] A. Faes, Z. Wuillemin, P. Tanasini, N. Accardo, J. Van Herle, Redox stable Ni–YSZ anode support in solid oxide fuel cell stack configuration, Journal of Power Sources 196 (2011) 3553–3558.

[22] J.L. Young, V.I. Birss, Crack severity in relation to non-homogeneous Ni oxidation in anode-supported solid oxide fuel cells, Journal of Power Sources 196 (2011) 7126–7135.

[23] T. Hatae, Y. Matsuzaki, S. Yamashita, Y. Yamazaki, Destruction modes of anode-supported SOFC caused by degrees of electrochemical oxidation in redox cycle, Journal of the Electrochemical Society 157 (2010) B650–B654.

[24] V. Vedasri, J.L. Young, V.I. Birss, A possible solution to the mechanical degradation of Ni–yttria stabilized zirconia anode-supported solid oxide fuel cells due to redox cycling, Journal of Power Sources 195 (2010) 5534–5542.

[25] S.H. Chan, X.J. Chen, K.A. Khor, A simple bilayer electrolyte model for solid oxide fuel cells, Solid State Ionics 158 (2003) 29–43.

[26] J. Ma, T.S. Zhang, L.B. Kong, P. Hing, S.H. Chan, $Ce_{0.8}Gd_{0.2}O_{2-\delta}$ ceramics derived from commercial submicron-sized CeO_2 and Gd_2O_3 powders for use as electrolytes in solid oxide fuel cells, Journal of Power Sources 132 (2004) 71–76.

[27] K.A. Khor, L.-G. Yu, S.H. Chan, X.J. Chen, Densification of plasma sprayed YSZ electrolytes by spark plasma sintering (SPS), Journal of the European Ceramic Society 23 (2003) 1855–1863.

[28] K. Chen, Z. Lu, N. Ai, X. Huang, Y. Zhang, X. Xin, R. Zhu, W. Su, Development of yttria-stabilized zirconia thin films via slurry spin coating for intermediate-to-low temperature solid oxide fuel cells, Journal of Power Sources 160 (2006) 436–438.

[29] Y. Du, N.M. Sammes, Fabrication of tubular electrolytes for solid oxide fuel cells using strontium- and magnesium-doped $LaGaO_3$ materials, Journal of the European Ceramic Society 21 (2001) 727–735.
[30] N.M. Sammes, G.A. Tompsett, H. Nafe, F. Aldinger, Bismuth based oxide electrolytes structure and ionic conductivity, Journal of the European Ceramic Society 19 (1999) 1801–1826.
[31] Y. Zhang, X. Huang, Z. Lu, Z. Liu, X. Ge, J. Xu, X. Xin, X. Sha, W. Su, A screen-printed $Ce_{0.8}Sm_{0.2}O_{1.9}$ film solid oxide fuel cell with a $Ba_{0.5}Sr_{0.5}Co_{0.8}Fe_{0.2}O_{3-\delta}$ cathode, Journal of Power Sources 160 (2006) 1217–1220.
[32] T. Inagaki, F. Nishiwaki, J. Kanou, S. Yamasaki, K. Hosoi, T. Miyazawa, M. Yamada, N. Komada, Demonstration of high efficiency intermediate-temperature solid oxide fuel cell based on lanthanum gallate electrolyte, Journal of Alloys and Compounds 408–412 (2006) 512–517.
[33] A. Sin, Y. Dubitsky, A. Zaopo, A.S. Arico, L. Gullo, D.L. Rosa, S. Siracusano, V. Antonucci, C. Oliva, O. Ballabio, Preparation and sintering of $Ce_{1-x}Gd_xO_{2-x/2}$ nanopowders and their electrochemical and EPR characterization, Solid State Ionics 175 (2004) 361–366.
[34] H.J. Park, G.M. Choi, Oxygen permeability of gadolinium-doped ceria at high temperature, Journal of the European Ceramic Society 24 (2004) 1313–1317.
[35] B. Timurkutluk, C. Timurkutluk, M.D. Mat, Y. Kaplan, Novel structured gadolinium doped ceria based electrolytes for intermediate temperature solid oxide fuel cells, Journal of Power Sources 196 (2011) 9361–9364.
[36] O.A. Marina, C. Bagger, S. Primdahl, M. Mogensen, A solid oxide fuel cell with a gadolinia-doped ceria anode: preparation and performance, Solid State Ionics 123 (1999) 199–208.
[37] A. Atkinson, Chemically induced stresses in gadolinium-doped ceria solid oxide fuel cell electrolytes, Solid State Ionics 95 (1997) 249–258.
[38] M. Mogensen, N.M. Sammes, G.A. Tompsett, Physical chemical and electrochemical properties of pure and doped ceria, Solid State Ionics 129 (2000) 63–94.
[39] K. Huang, J.H. Wan, J.B. Goodenough, Increasing power density of LSGM-based solid oxide fuel cells using new anode materials, Journal of the Electrochemical Society 148 (2001) A788–A794.
[40] K. Huang, J.B. Goodenough, A solid oxide fuel cell based on Sr- and Mg-doped LaGaO electrolyte: the role of a rare-earth oxide buffer, Journal of Alloys and Compounds 303–304 (2000) 454–464.
[41] X. Zhang, S. Ohara, R. Maric, H. Okawa, T. Fukui, H. Yoshida, T. Inagaki, K. Miura, Interface reactions in the NiO–SDC–LSGM system, Solid State Ionics 133 (2000) 153–160.
[42] K. Huang, J.B. Goodenough, Oxide-ion conducting ceramics for solid oxide fuel cells, Journal of Materials Science 36 (2001) 1093–1098.
[43] D. Lee, I. Lee, Y. Jeon, R. Song, Characterization of scandia stabilized zirconia prepared by glycine nitrate process and its performance as the electrolyte for IT-SOFC, Solid State Ionics 176 (2005) 1021–1025.
[44] J.W. Fergus, Electrolytes for solid oxide fuel cell, Journal of Power Sources 162 (2006) 30–40.
[45] C. Haering, A. Roosen, H. Schichl, M. Schnöller, Degradation of the electrical conductivity in stabilised zirconia system. Part II: Scandia-stabilised zirconia, Solid State Ionics 176 (2005) 261–268.
[46] Y. Arachi, H. Sakai, O. Yamamoto, Y. Takeda, N. Imanishai, Electrical conductivity of the ZrO_2–Ln_2O_3 (Ln = lanthanides) system, Solid State Ionics 121 (1999) 133–139.
[47] R. Chiba, F. Yoshimura, J. Yamaki, T. Ishii, T. Yonezawa, K. Endou, Ionic conductivity and morphology in Sc_2O_3 and Al_2O_3 doped ZrO_2 films prepared by the sol–gel method, Solid State Ionics 104 (1997) 259–266.
[48] N. Orlovskaya, S. Lukich, G. Subhash, T. Graule, J. Kuebler, Mechanical properties of 10 mol% Sc_2O_3–1 mol% CeO_2–89 mol% ZrO_2 ceramics, Journal of Power Sources 195 (2010) 2774–2781.
[49] S. Yarmolenko, J. Sankar, N. Bernier, M. Klimov, J. Kapat, N. Orlovskaya, Phase stability and sintering behavior of 10 mol% Sc_2O_3–1 mol% CeO_2–ZrO_2 ceramics, Fuel Cell Science Technology 6 (2009) 1–8.
[50] S.P.S. Badwal, Stability of solid oxide fuel cell components, Solid State Ionics 143 (2001) 39–46.
[51] Z. Wang, M. Cheng, Z. Bi, Y. Dong, H. Zhang, J. Zhang, Z. Feng, C. Li, Structure and impedance of ZrO_2 doped with Sc_2O_3 and CeO_2, Materials Letters 59 (2005) 2579–2582.
[52] D.S. Lee, W.S. Kim, S.H. Choi, J. Kim, H.W. Lee, J.H. Lee, Characterization of ZrO_2 co-doped with Sc_2O_3 and CeO_2 electrolyte for the application of intermediate temperature SOFCs, Solid State Ionics 176 (2005) 33–39.
[53] Y. Arachi, T. Asai, O. Yamamoto, Y. Takeda, N. Imanishi, K. Kawate, C. Tamakoshi, Electrical conductivity of ZrO_2-Sc_2O_3 doped with HfO_2 CeO_2, and Ga_2O_3, Journal of the Electrochemical Society 148 (2001) A520–A523.
[54] Y. Mizutani, M. Tamura, M. Kawai, O. Yamamoto, Development of high-performance electrolyte in SOFC, Solid State Ionics 72 (1994) 271–275.
[55] T.J. Bastow, T. Mathews, J.R. Sellar, Al_2O_3 solubility in the fast ion conductor $0.88ZrO_2$–$(0.12-x)Sc_2O_3$–xAl_2O_3 determined by ^{27}Al NMR, Solid State Ionics 175 (2004) 415–417.
[56] J.W. Kim, A.V. Virkar, K.Z. Fung, K. Mehta, S.C. Singhal, Polarization effects in intermediate temperature, anode-supported solid oxide fuel cells, Journal of Electrochemical Society 146 (1999) 69–78.
[57] M. Hirano, M. Inagaki, Y. Mizutani, K. Nomura, M. Kawai, Y. Nakamura, Improvement of mechanical and electrical properties of scandia-doped zirconia ceramics by post-sintering with hot isostatic pressing, Journal of the American Ceramic Society 83 (2000) 2619–2621.
[58] Y.J. Leng, S.H. Chan, K.A. Khor, S.P. Jiang, Performance evaluation of anode-supported solid oxide fuel cells with thin film YSZ electrolyte, International Journal of Hydrogen Energy 29 (2004) 1025–1033.
[59] P. Dahl, I. Kaus, Z. Zhao, M. Johnsson, M. Nygren, K. Wiik, T. Grande, M.A. Einarsrud, Densification and properties of zirconia prepared by three different sintering techniques, Ceramics International 33 (2007) 1603–1610.
[60] K. Rajeswari, M.B. Suresh, D. Chakravarty, D. Das, R. Johnson, Effect of nano-grain size on the ionic conductivity of spark plasma sintered 8YSZ electrolyte, International Journal of Hydrogen Energy 37 (2012) 511–517.
[61] M. Mazaheri, A.M. Zahedi, M.M. Hejazi, Processing of nanocrystalline 8 mol% yttria-stabilized zirconia by conventional microwave-assisted and two-step sintering, Materials Science and Engineering A 492 (2008) 261–267.
[62] J. Mencik, Strength and fracture of glass and ceramics, European Journal of Glass Science and Technology Part A 12 (1992) 164–168.